Computational Materials Science 242 (2024) 113077

Contents lists available at ScienceDirect

Computational Materials Science

journal homepage: www.elsevier.com/locate/commatsci

Full length article

Machine-learning enhanced thermal stability investigation of single Shockley stacking faults in 4H-SiC

Haonan Chen, Wenyu Kang *, Wei Lin, Junyong Kang *

College of Physical Science and Technology, Tan Kah Kee Innovation Laboratory (FDIX), School of Electronic Science and Engineering, College of Chemistry and Chemical Engineering, Xiamen University, Xiamen, 361005, Fujian, China

ARTICLE INFO

Dataset link: https://github.com/CHN-beta/ufo

Keywords:
Machine learning force field
Basal plane dislocations
First principle calculations
Molecular dynamics
Defects evolution
Phonon spectra

ABSTRACT

A comprehensive understanding of single Shockley stacking faults (1SSFs) would be crucial for defect control in silicon carbide (SiC). Nevertheless, the thermal stability of 4H-SiC 1SSFs remains unclear due to limitations in conventional technologies. In this work, a machine learning force field (MLFF) for the Si-C system was developed, and the outcomes were compared with other simulations and experiments in three aspects. The MLFF was then utilized to investigate the thermal stability of ten established 1SSF models (3072 atoms for each) at seven temperatures. The results revealed that antiphase boundaries (APBs) positively related to thermal stability, and APB-lacking 1SSFs susceptible to annihilation. Among the stably existing 1SSFs, a bidirectional transition process of 30° partial dislocations (PDs) between symmetric reconstruction (SR) and asymmetric reconstruction (AR) was visualized. The distorted bilayers caused by 90° PDs were also observed. Notably, two novel structures were identified with robust thermal stability that could naturally exist in 4H-SiC. Additionally, the specific vibration modes of 1SSFs in phonon spectra were characterized, which offers potential applications in non-destructive defect detection in SiC materials. This study provides advanced insights into the evolution and thermal stability of 1SSFs at the atomic level.

1. Introduction

SiC is a promising wide-bandgap semiconductor material with high critical electric field strength and high thermal conductivity. It has been widely used in power electronic devices and has long attracted a lot of research [1,2]. SiC has more than 250 polytypes [3], the 3C-SiC has been widely studied in the past decades [4–13]. Currently, the 4H-SiC has gradually received more attention than other polytypes, thanks to the development of epitaxy technology and the increasing application in the new energy industry [14–16]. The 4H-SiC has a wider bandgap, higher critical electric field strength, higher thermal conductivity, and higher electron mobility along the *c*-axis than other polytypes. It shows an exclusive application in power electronic devices, such as the Schottky barrier diodes and the power metal–oxide–semiconductor field-effect transistors [17,18]. However, these applications are negatively affected by Shockley stacking faults (SSFs), which are a class of common defects in 4H-SiC.

The structure of SiC could be considered as a stack of Si and C atomic layers, and only the stacking sequence of exactly repeating A-B-C-B leads to the formation of 4H-SiC without defects. The differences in formation energies between different stacking positions are only about 1 meV/atom [6], leading to a mass formation of SSFs in 4H-SiC. One of the most common SSFs in 4H-SiC is the 1SSF bounded by two PDs [19,20], which has an extremely low formation energy of approximately 15 mJ/m^2 [21]. The 1SSFs and corresponding PDs are usually formed during the material growth or device fabrication by decomposition of basal plane dislocations (BPDs) [19,22], and they could subsequently expand during the usage influenced by multiple factors (such as electric current [23–25], high-temperature annealing [26], or ultraviolet irradiation [20,27]). The expansion of 1SSFs would greatly increase the forward voltage and lead to the degradation of the performance of 4H-SiC devices [28]. Therefore, numerous studies have been carried out to understand the nature of 1SSFs and PDs.

Abbreviations: 1SSF, single Shockley stacking fault; SiC, silicon carbide; MLFF, machine learning force field; APB, antiphase boundary; PD, partial dislocation; SSF, Shockley stacking fault; BPD, basal plane dislocation; STEM, scanning transmission electron microscopy; MD, molecular dynamics; VASP, Vienna Ab-initio Simulation Package; PBE, Perdew–Burke–Ernzerhof; PAW, projector-augmented wave; DoS, density of states; LAMMPS, Large-scale Atomic/Molecular Massively Parallel Simulator; GW, Gao-Weber; GW_ZBL, Gao-Weber with Ziegler–Biersack–Littmark universal screening function; MEAM, modified embedded-atom potential; MEAM_Kang, MEAM modified by Kang et al.; EDIP, environment-dependent interatomic potential; SR, symmetric reconstruction; AR, asymmetric reconstruction

* Corresponding authors.
E-mail addresses: wykang@xmu.edu.cn (W. Kang), jykang@xmu.edu.cn (J. Kang).

https://doi.org/10.1016/j.commatsci.2024.113077
Received 28 December 2023; Received in revised form 23 April 2024; Accepted 1 May 2024
Available online 13 May 2024

Savini et al. proposed eight possible structures of PDs (four for C-core and four for Si-core) in 4H-SiC in 2007. They studied the bond length between atoms in PDs, as well as the formation energy and band structures of PDs. Simultaneously, they discussed the effect of Fermi level on the stability of PDs, and suggested that the rotation in the basal plane of atoms in PDs is the reason for the migration of PDs and the expansion of 1SSFs [29]. In the following decade, many experiments on SSFs in 4H-SiC were conducted. The 4H-SiC wafers with SSFs were fabricated, and the morphology and Burgers vectors of SSFs and PDs were observed at the micron scale [20,27,30]. In 2020, Nishio et al. investigated the structure of PDs allocated surrounding a single 1SSF at the atomic scale by scanning transmission electron microscopy (STEM), and proposed possible structures of the 1SSF and PDs based on their observations [19]. Nevertheless, all published structures of PDs and 1SSFs only included the atomic offset in the basal plane, but the Shockley-type defects with off-plane displacement still need to be considered. Moreover, the published literature demonstrated the stability of PDs without considering temperature, while the thermal effect on the stability also needs to be investigated.

This work firstly explored the thermal stability of 1SSFs in 4H-SiC by developing an MLFF of the Si-C system, which enabled the simulations to be performed on larger models with thermal effects involved. This MLFF was verified in comparison with other simulations and experiments. The thermal stability and evolution of 1SSFs were characterized and demonstrated. The specific vibration modes of 1SSFs in phonon spectra were profiled in order to explore a non-destructive defect detection technology in SiC materials.

2. Method

2.1. Establishment of different 1SSF models

In this work, all 1SSF models were established with three edges along the $[11\bar{2}0]$, $[\bar{1}100]$, and [0001] directions. Different types of 1SSF were denoted as D_{ij} according to constructing procedures, where i denoted the atomic bilayer containing the 1SSF and j denoted the transformation method of atom coordinates to construct the initial structure of the 1SSF. Two different atomic bilayers were considered ($i \in \{1,2\}$) according to the symmetry of the 4H-SiC lattice (space group of $P6_3mc$ [31,32]), and five different transformation methods were used ($j \in \{1,2,3,4,5\}$) in each bilayer.

The models used to train the force field were established in size 12.32 Å × 21.34 Å × 10.08 Å and contained 256 atoms (Fig. 1a), and the D_{11}-D_{15} and the D_{21}-D_{25} were constructed by transforming the coordinates of atoms in two different atomic bilayers (purple and green shadows in Fig. 1b, respectively). The purple-noted bilayer was further illustrated from a top view (Fig. 1c) to show the detailed procedure of constructing D_{11}-D_{15}. The D_{11} was obtained by translating the selected atoms (darker-colored in Fig. 1c) by $\frac{1}{6}[11\bar{2}0]$ (Fig. 1d and the bubble on the left), and the D_{12} was obtained by exchanging the x and y coordinates of Si atoms with those of C atoms among the selected atoms (Fig. 1e and the bubble on the left). D_{13}-D_{15} were obtained from the D_{12}, by translating the selected atoms in $\frac{1}{3}[\bar{1}100]$, $\frac{1}{3}[1\bar{1}00]$, and $\frac{1}{3}[0001]$, respectively, and then inserting and removing atoms close to the boundaries according to the atomic arrangement (Fig. 1f–h). The construction of D_{21}-D_{25} followed the similar way but transforming the coordinates of atoms in the green-noted bilayer in Fig. 1b (details were shown in supplementary Fig. A.1). After training the MLFF, ten models were established based on the same procedure in a 3072-atom size (24.64 Å×42.68 Å×30.25 Å) for subsequent 1SSFs evolution investigation (Fig. 1i). Meanwhile, the boundary effect was considered, only 5 Å distance (about two atomic layers) could be influenced by the periodic boundaries, but the 1SSF layers in all 3072-atom models were at least 10 Åfar from each boundary.

2.2. Training and utilizing MLFF

The MLFF was firstly trained by performing on-the-fly MLFF molecular dynamics (MD) following a designed workflow. Then, the trained MLFF was further utilized in comparison with other methods (including simulations and experiments) and investigation of 1SSF evolutions.

In the training process, hundreds of on-the-fly MLFF MD simulations were performed using the Vienna Ab-initio Simulation Package (VASP) [34], and the detail of a single simulation is shown in Fig. 2a. An initial MLFF was obtained in the first several MD steps, by performing ab initio MD in these steps to generate the training data (atomic structures and corresponding energies and forces), and then training the MLFF with a basis selected from the local configurations (local surroundings of each atom) in the training data. The MLFF was continuously updated in the following MD steps, by comparing the prediction error of the MLFF (estimated using Bayesian linear regression [35]) with an artificially set threshold in each step, and if the error was higher than the threshold, ab initio calculations would be performed to update the training data and MLFF. Moreover, multiple MLFFs trained in different simulations could be merged into a single MLFF by merging the training data and then retraining an MLFF with the merged training data. Besides, the implementation in VASP includes additional features to improve program robustness and reduce computational costs, and the details could be found in the study by Jinnouchi et al. [36,37] and in the VASP manual [38]. Two additional adjustments were made in this work to reduce the memory consumption during the training process. The threshold for the CUR algorithm [39] used in the sparsification of the basis [40] was relaxed to 10^{-8}, and structures that did not contribute to the basis were discarded after each merge of training data. Each on-the-fly MLFF MD simulation was performed for 2×10^3 MD steps with a step size of 1 fs, and the motion of the ionic and lattice degrees of freedom followed the NpT ensemble proposed by Parrinello et al. [41] and the Langevin equation [42]. The friction coefficients for Si, C, and lattice degrees of freedom were set to $3\,ps^{-1}$, $3\,ps^{-1}$, and $0\,ps^{-1}$, respectively. The ab initio calculations were performed with the Perdew–Burke–Ernzerhof (PBE) exchange energy [43], projector-augmented wave (PAW) representation [44] and periodic boundary conditions. A cutoff energy of 520 eV was used, and the Brillouin zone was sampled at only the Γ point.

The MLFF was trained following a designed workflow (Fig. 2b), where the MLFF was first trained with the defect-free 4H-SiC model at a temperature of 2000 K (the upper box) and continuously trained with the 1SSF models (the lower box). The training process on the 1SSF models was performed in several turns, and in each turn, ten different 1SSF models (D_{11}-D_{15} and D_{21}-D_{25}) were simulated at seven different temperatures (300 K, 600 K, 900 K, 1200 K, 1500 K, 1800 K, and 2000 K). At the end of each turn, the training data obtained from the same 1SSF model were merged and used continuously into the next turn. The training progress was monitored by the number of local configurations in the bases used to train the MLFF, and the training process was terminated after eight turns, where the average variation of the numbers of local configurations for all models reached below zero at the last turn. Finally, the MLFF was obtained by merging the training data from all the 1SSF models and used for the subsequent comparisons and simulations.

The outcomes from trained MLFF were compared with other simulations and experiments in three aspects (Fig. 2c), including the elasticity tensor, the 1SSF formation energies, and the phonon density of states (DoS). The simulations performed for comparison including both calculations using the ab initio method and calculations using conventional force fields. The ab initio calculations were performed using VASP [34], with the PBE exchange energy [43], PAW representation [44], and a cutoff energy of 400 eV. The calculations using conventional force fields were performed using the Large-scale Atomic/Molecular Massively Parallel Simulator (LAMMPS) [45], and the force fields considered including Tersoff_1989 [46], Tersoff_1990 [47], Tersoff_1994 [48],

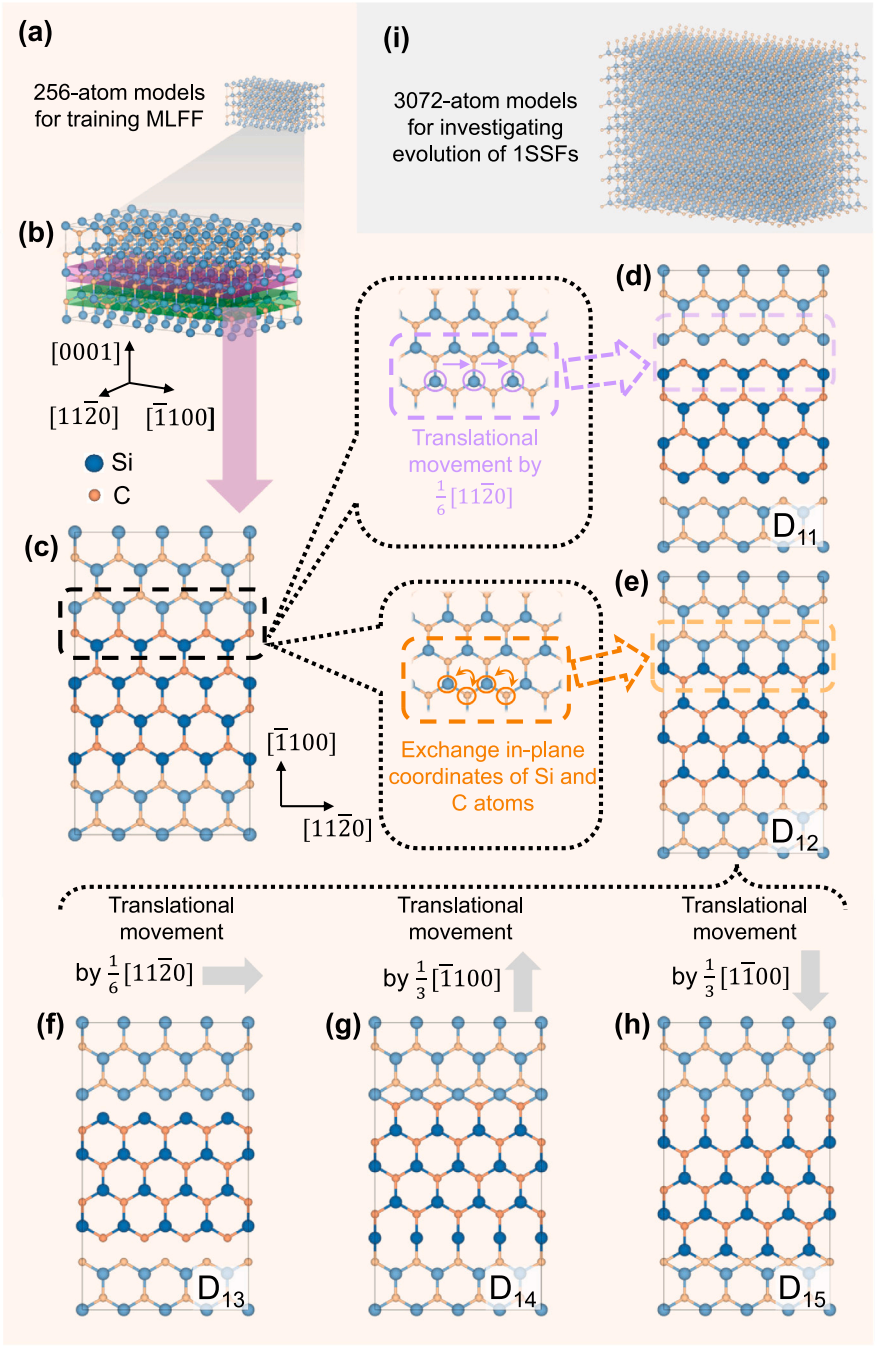

Fig. 1. The steps to construct the initial structures of different 1SSF models. (a) The 256-atom model of 4H-SiC, which was used to train the force field. (b) Magnified view of (a). The purple and green shadows represent the bilayers we used to construct D_{11}-D_{15} and D_{21}-D_{25}, respectively. (c) The top view of the bilayer marked by the purple shadow in (b). The darker colors were used to highlight the atoms that were moved during the construction of the 1SSF models. (d–h) The top views of the atomic layers containing 1SSFs in the 256-atom models of D_{11}-D_{15}. (i) The 3072-atom model of 4H-SiC, which was used to investigate the evolution of defects with trained MLFF. The visualization of atomic structures was performed using VESTA [33].

Tersoff_Erhart-Albe [49], Gao-Weber (GW) [50], GW with Ziegler–Biersack–Littmark universal screening function (GW_ZBL) [50,51], modified embedded-atom potential (MEAM) [52,53], MEAM modified by Kang et al. (MEAM_Kang) [54], Vashishta [13], and environment-dependent interatomic potential (EDIP) [55]. To calculate the elasticity tensor of the defect-free 4H-SiC, the finite difference approach [56,57] was used with different sizes of models (2880-atom model in size 30.80 Å×32.01 Å×30.25 Å for calculations using MLFF and conventional force fields, and a single unit cell for the calculations using the ab initio method). The experiment results from the work of Kamitani et al. [58] were used as the standard reference in the comparison. Meanwhile, in ab initio calculations, the k-point mesh was set to 8 × 8 × 5, and the break conditions for electronic self-consistency and ionic relaxation loops were narrowed to 1×10^{-9} eV and 1×10^{-8} eV, respectively. To calculate the 1SSF formation energies, 256-atom models were used in all methods for consistency, and a k-point mesh of 2 × 1 × 2 was used in ab initio calculations. To calculate the phonon DoS of the defect-free 4H-SiC and the 1SSF models, two different approaches were used in different methods, and 256-atom models were used in all methods to keep consistency. Firstly, in the calculations using MLFF

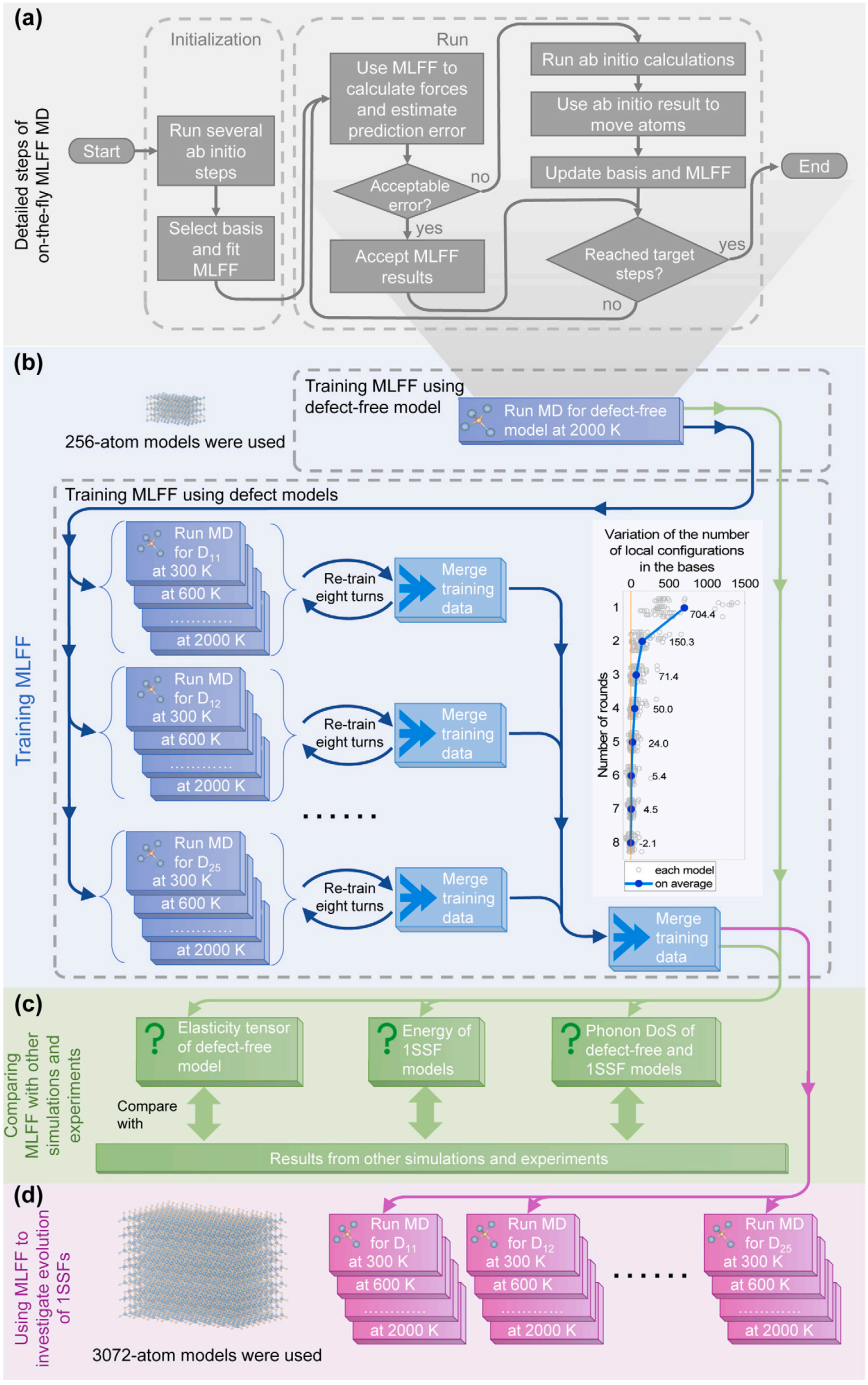

Fig. 2. Simulation scheme used in this work. (a) A typical workflow of MD with on-the-fly MLFF. (b) Workflow of training MLFF in this work. (c) Comparing MLFF simulation results with other simulations and experiments. (d) Investigating the evolution of 1SSFs using the trained MLFF.

and conventional force fields, MD simulations were performed for 1.1×10^5 steps at a temperature of 300 K, and the phonon DoS was obtained through the Fourier transformation of the trajectories in the last 1×10^5 steps. Secondly, the finite difference approach [56,57] was used in the ab initio calculations (because the ab initio MD simulations were too computationally expensive), and the Phonopy package [59,60] was used to generate structures with displacements (32 structures for the defect-free model and 1536 structures for each 1SSF model). These two approaches would lead to different peak heights between the acoustic phonon DoS and the optical one, but the peak positions should not be affected, because the finite difference approach took all possible phonon modes into account, while the Fourier transformation of MD trajectories only counting the phonon modes occupied at a finite temperature (300 K in our simulations). In the calculations of the 1SSF formation energies and phonon DoS of 1SSF models, two structures were taken into consideration (including the final structures of D_{12} and D_{14}), due to other 256-atom 1SSF models were unstable under the temperature of 300 K (including D_{11}, D_{13}, D_{21} and D_{23}) or yielded similar results to D_{12} (including D_{22}) or D_{14} (including D_{15}, D_{24}, and D_{25}). Besides, the phonon spectrum of the defect-free 4H-SiC was also calculated using ab initio method for comparison with the phonon DoS [56,57,59,60].

The MLFF was subsequently used to investigate the evolution of 1SSFs (Fig. 2d), and all models were scaled up to 3072-atom size

(24.64 Å × 42.68 Å × 30.25 Å) with more simulation steps. These simulations were all performed for 1×10^5 steps, with the same settings mentioned above.

2.3. Definition of elasticity tensor

The definition of subscripts in elasticity tensor varies between different software (i.e., VASP and LAMMPS), potentially causing confusion. To provide clarity, the elasticity tensor $C_{ij,kl}$ in this work is defined as a fourth-order tensor relating the stress T_{ij} to the strain E_{kl} in a linear approximation:

$$T_{ij} = \sum_{k,l} C_{ij,kl} E_{kl}, \tag{1}$$

where i, j, k, and l denote the Cartesian coordinates x, y, and z. The elasticity tensor contains at most 36 independent components, and in particular, there are only 5 independent components for hexagonal crystals (such as 4H-SiC), specifically $C_{xx,xx}$, $C_{xx,yy}$, $C_{xx,zz}$, $C_{zz,zz}$, and $C_{yz,yz}$ [61].

2.4. Specific vibration modes of 1SSFs on phonon spectra

For analyzing the vibration modes of 1SSFs, the phonon spectra were calculated on supercells containing 256 atoms using the Phonopy package [59,60] and then transformed into primitive cells (i.e. unfolding of the phonon spectra). This unfolding process was necessary because the phonon spectra of the supercells were too dense to resolve. An approximation was used to deal with the translational symmetry broken caused by 1SSF, which was derived from the work of Zheng and Zhang [62] with two optimizations. Firstly, the projection coefficients of different modes were calculated parallelly, with the values of plane-wave bases on all atoms calculated in advance, and thus the computational time was dramatically reduced. Secondly, the coordinates of unfolded q-points were calculated directly instead of searching in a pre-defined range, which made the procedure adaptive to supercells in any shape and size. This was achieved by decomposing the transformation matrix between the supercell lattice and the primitive cell lattice into a series of integer elementary matrixes. Each of the integer elementary matrixes represented a simplified translation of the lattice vectors (multiplying an integer on a single lattice vector, swapping of two lattice vectors, or adding a lattice vector onto another lattice vector), and thus the coordinates of unfolded q-points could be calculated using these elementary matrixes. In addition, the intensities of phonon modes were estimated by the sum of the squared norm of the projection coefficients corresponding to each mode, where the sum was taken over all the calculated modes within the frequency range of ±0.05 THz at the same q-point in the primitive cell and from a single q-point in the supercell. The vibration modes of 1SSFs in the phonon spectra were profiled by projecting the phonon modes on the atoms both in defects and bonded to defects.

3. Result and discussion

3.1. Comparing MLFF outcomes with other simulations and experiments

To evaluate the accuracy of the trained MLFF, the MLFF outcomes were compared with other simulations and experiments on three aspects, including the elasticity tensor of the defect-free 4H-SiC, the 1SSF formation energies, and the phonon DoS of both the defect-free 4H-SiC and the 1SSF models. There were two training outcomes in the comparison, including the preliminary trained MLFF (trained with the defect-free model only) and the final MLFF (trained with both the defect-free model and 1SSF models).

Calculated elasticity tensors of the defect-free 4H-SiC were shown in Fig. 3a, and the experimental result was used as a standard reference when comparing results with different methods. The MLFF showed remarkable accuracy with an average error below 5%. Among the conventional force fields, besides Tersoff_Erhart-Albe, the others showed different results with the ab initio calculations and the experimental result. The 1SSF formation energies were also calculated (Fig. 3b), where the final MLFF showed almost the same results as the ab initio calculations. Importantly, the preliminary trained MLFF failed to predict 1SSF properties especially for D_{12} (Fig. 3c), where the predicted C–C bonds had nearly zero length. Therefore, it was necessary to train MLFF with 1SSFs.

The phonon DoS of the defect-free 4H-SiC and two 1SSF models were also calculated and shown in Fig. 4. The final MLFF was continuously in light with ab initio results for the peak frequency of the phonon DoS of both the defect-free model and the 1SSF models.

There were two key factors contributing to the difference between the outperformed MLFF and conventional force fields. Firstly, conventional force fields relied on pre-defined functions with a limited number of fitting parameters (< 50 in this work) to describe interatomic interactions, whereas the MLFF employed selected local configurations as basis functions with much more fitting parameters (10501 in this work, detailed in Section 2.2 and Ref. [36,37]). Therefore, the MLFF was not limited by any pre-defined functions, providing greater flexibility to describe 1SSF structures. Secondly, conventional force fields usually use short cutoff distances (e.g., < 3 Å in Tersoff-based methods [46–50], making it failed to distinguish different SiC polytypes [46]). In contrast, the MLFF used longer cutoff distances (5 Å for angular descriptors and 8 Å for radial descriptors [36,37]), enabling it to capture more atoms within local configurations and thus improve accuracy. Therefore, the final MLFF was suitable to be used in predicting multiple properties of 4H-SiC and investigating the evolution of 1SSFs. Additionally, the MLFF had much lower computational costs compared to ab initio calculations, for instance, ab initio calculations took about ten hours but MLFF calculations took only about 0.3 s in the case of running a single step of an MD simulation on a model containing 3072 atoms with 28 CPU cores. Thus, by using MLFF, the model size could be scaled up and the simulation steps could be extended, which brings the SiC simulations closer to real-world conditions.

3.2. Evolution of different defects

The MLFF was used to study defect evolution in ten 3072-atom 4H-SiC models (D_{11}-D_{15} and D_{21}-D_{25}) through MD simulations at seven different temperatures. The evolution of the ten models was categorized into two groups according to their thermal stability characterization, i.e., the unstably and stably existing defects.

3.2.1. Unstably existing defects

The unstably existing defects were identified according to the spontaneous annihilation of the extended defects under thermal effects. The D_{11} and D_{21} belonged to this group, and both of them lacked APB (but the other 1SSF models had APBs). For a more comprehensive illustration, the evolution process of D_{11} at 300 K was decomposed into several stages (Fig. 5). The 1SSF in the initial structure lacked bonding to the atoms in the upper and lower atomic layers as well as to the surrounding atoms at the boundaries. This absence of bondings resulted in the free slip of the atoms in both directions even with a slight disturbance, which was supported by our simulations with different random seeds. In one of these simulations, the trajectory of a C atom displayed a slight slip at about 25 fs and formed a weak covalent bond with a Si atom in the lower layer (highlighted by red arrows). This bond caused adjacent atoms in 1SSF to slide in the same direction (highlighted by red boxes), and finally at 300 fs, the majority of the atoms in the 1SSF reached their defect-free positions. The spontaneous annihilation of 1SSFs in D_{11} and D_{21} revealed that APB-lacking 1SSFs were unstable under thermal effects. Therefore, the 1SSFs lacking APB required less attention in real SiC growth because they could spontaneously annihilate in growth temperature.

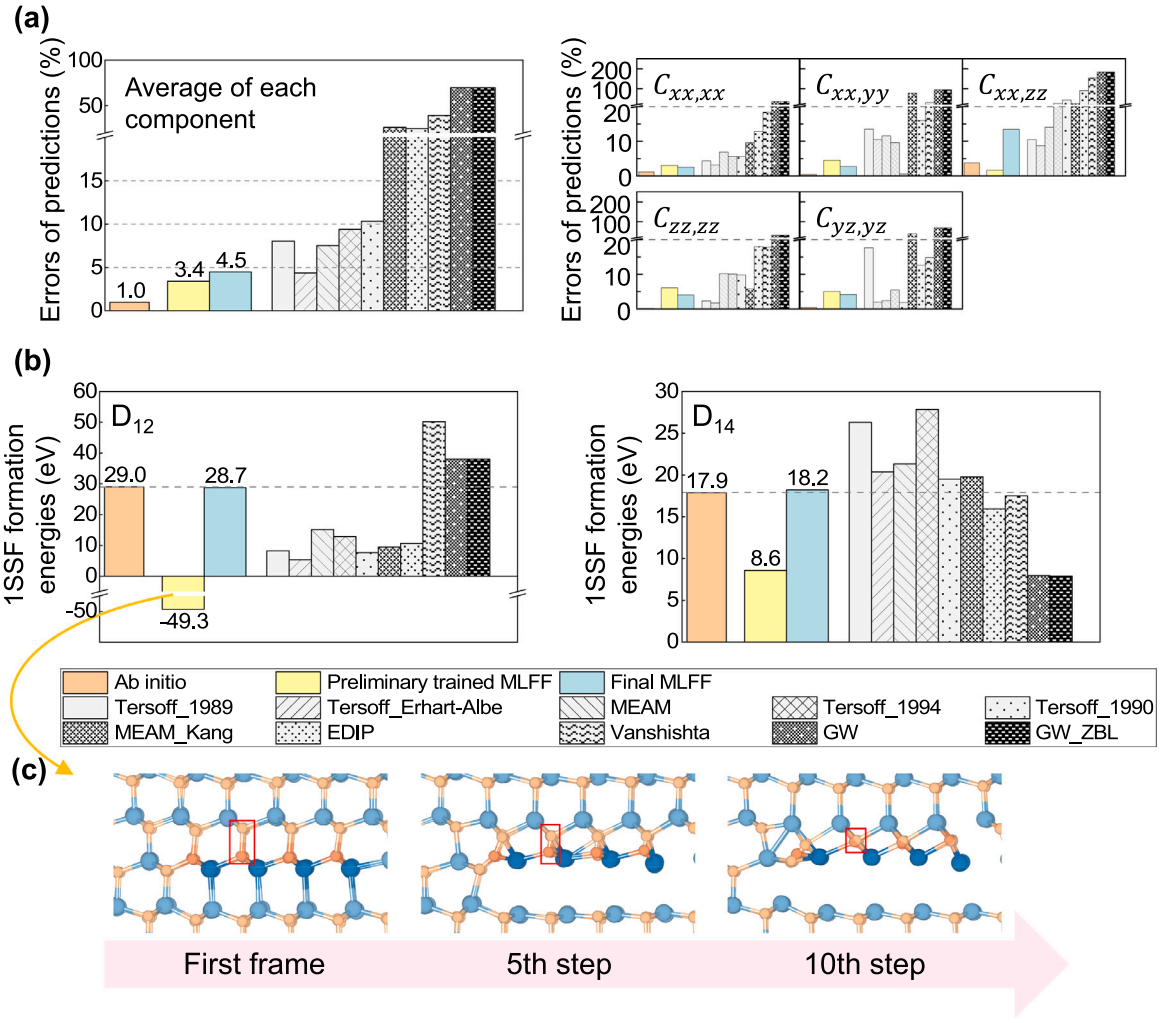

Fig. 3. (a) Errors of computed elasticity tensors of the defect-free 4H-SiC compared to the experimental result. (b) The 1SSF formation energies of the final structure of D_{12} and D_{14}. (c) The first few frames of the relaxation process of D_{12} using the preliminary trained MLFF.

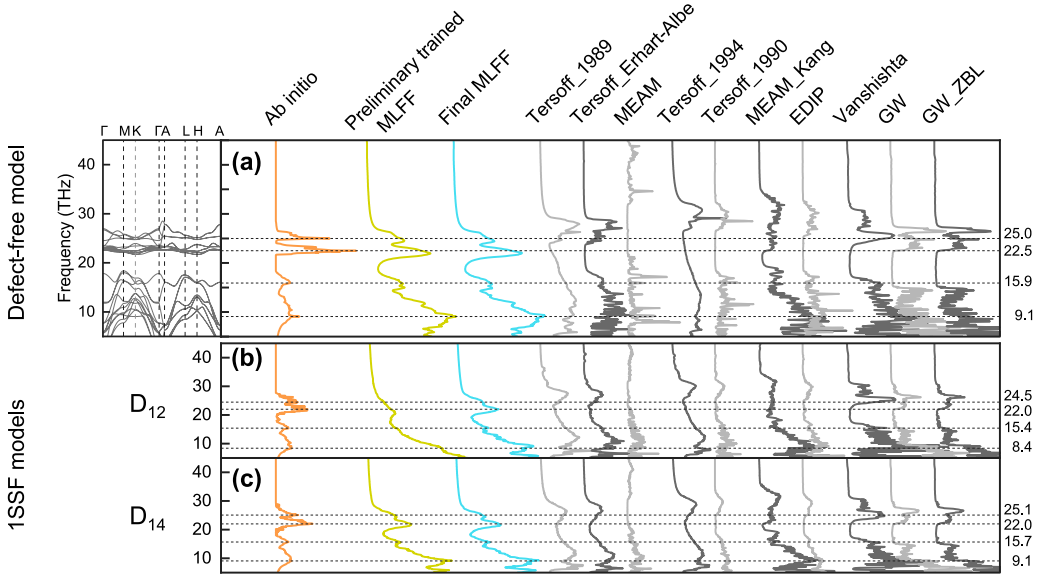

Fig. 4. Phonon DoS of (a) the defect-free 4H-SiC and the final structure of (b) D_{12} and (c) D_{14} obtained by various methods. The dashed line in each plot denotes the peak frequency of the ab initio results.

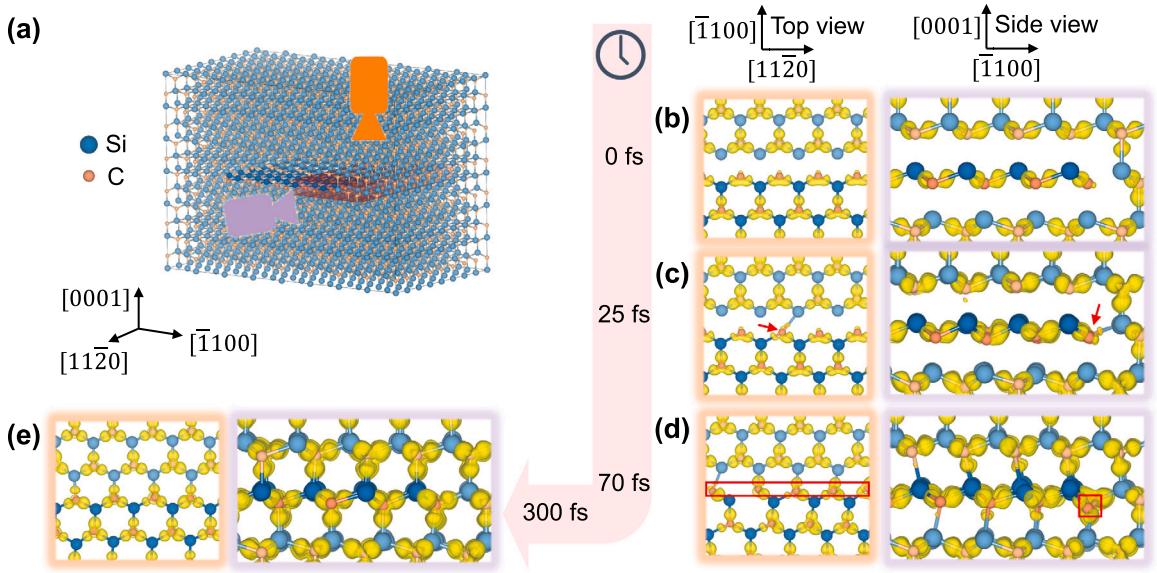

Fig. 5. The evolution of D_{11} in one of the simulations at 300 K. (a) A full view of the initial structure, where the two cameras show the two viewpoints. (b)–(e) The top view and side view at 0 fs, 25 fs, 70 fs, and 300 fs, respectively. The differential charge density is displayed as a yellow isosurface to represent the values of 0.02 e/Å^3. For clarity, the charge depletion is not shown.

3.2.2. Stably existing defects

The defects of D_{12}-D_{15} and D_{22}-D_{25} were classified as stably existing defects according to the persistence (the extended defects remained after 1×10^4 MD simulation steps, which went through enough time of relaxation under different correlated temperatures). Among these defects, D_{13}-D_{15} and D_{23}-D_{25} formed structures that were in light with published literature, and D_{12} and D_{22} formed structures that were newly discovered in this work.

The evolutions of D_{14}, D_{24}, D_{15}, and D_{25} were similar to each other, thus only the evolution of D_{14} was discussed in detail. The evolution process of D_{14} was slightly different at two temperature ranges (i.e., 1500 K or below, and 1800 K or above), and an example for 1500 K or below were demonstrated by the evolution process of the C-core in D_{14} at the temperature of 300 K (Fig. 6a–d). In the initial structure, no bonds were formed between the C atoms in the 1SSF and the atoms in the lower atomic layer. Thus, the C atoms oscillated under thermal effects and formed several covalent bonds with the Si atoms in the lower layer at 50 fs (highlighted by the red box), subsequently causing adjacent atoms in 1SSF to form similar covalent bonds at 500 fs. Finally, two weak C–C bonds were formed at about 600 fs (one of them was marked by the red box). Meanwhile, the Si-core underwent a similar process and formed similar structures. The structures of the C-core at 500 fs and 600 fs were previously reported by Savini et al. as 30° SR PDs and 30° AR PDs, respectively [29]. At temperatures of 1500 K or below, the structure of D_{14} finally set in still as 30° AR PDs, which was consistent with the findings that 30° AR PDs had lower energies than 30° SR PDs [29]. However, at temperatures of 1800 K or above, the structures could randomly transform between SR and AR PDs, with the size of 1SSFs consistently remaining unchanged during the transformation. Therefore, D_{14} and others in type of 1SSFs were considered to have remarkable stability at both temperature ranges. In addition, the structure of 30° PDs could be interpreted as a mis-stacking of Si-C pairs (Fig. 6e), which was in agreement with the STEM observations [19]. Our work underscored that the 1SSFs of D_{14}, D_{24}, D_{15} and D_{25} (existing as 30° PDs) had thermal stability under high temperatures, which means they could not be eliminated simply by using the high-temperature annealing at the end of physical vapor transport bulk growth or at the beginning of the chemical vapor deposition epitaxy.

The evolution processes of D_{13} and D_{23} were similar to each other, and the evolution of D_{13} under 300 K was demonstrated as an example (Fig. 7a–b). The initial structure of D_{13} was mentioned as 90° SR PDs in the work of Savini et al. [29], but it was not stable in our simulations and could transform into 90° AR PDs with kinks. Further, these kinks could migrate along the 1SSFs at the temperatures of 1200 K or above. The migration of kinks was considered highly correlated with the expansion or shrinkage of the 1SSF [29], indicating that the 90° PD structures might be less stable than 30° PDs at high temperatures. Meanwhile, the 90° PD structures, like the 30° PDs, could also be considered as a mis-stacking of Si-C pairs. Moreover, 90° PDs caused further distortion in adjacent atomic layers (Fig. 7c–d for D_{13} and Fig. 7e–f for D_{23}). Our found distortion can be used to explain the STEM observations from Johji et al. [19], and potentially hold implications for the quality of 4H-SiC epitaxial growth. Our work shows that the 1SSFs of D_{13} and D_{23} could be present as 90° AR PDs with kinks under thermal effects, and highlighted the distortion of atomic layers induced by the 90° PDs for the first time.

The structures of D_{12} and D_{22} had not been previously reported in the literature. This is the first report of both of them having steady thermal stability, and been identified by flipped Si-C atomic layers in the 1SSFs. The evolution process of D_{12} is shown in Fig. 8a–c, where C and Si atoms in the 1SSF started to move upwards and downwards at the beginning of the simulation, respectively, and subsequently formed C–C and Si–Si bonds with the atoms in the upper and lower atomic layers (highlighted by the purple and green boxes, respectively). The stability of the flipped structure persisted across D_{12} and D_{22} at temperatures ranging from 300 K to 2000 K (Fig. 8d-e), thanks to the robust C–C and Si–Si bonds formed between the 1SSF and the adjacent atomic layers. The formation energies of the newly formed structures were calculated to be 103.15 eV for D_{12} and 109.96 eV for D_{22}. In comparison, the formation energies of D_{13}, D_{23}, D_{14}, D_{24}, D_{15}, and D_{25} in the same size of supercell were 62.58 eV, 68.95 eV, 91.31 eV, 51.03 eV, 62.34 eV, and 58.29 eV, respectively. The consistent energy magnitudes across all structures suggested that these new configurations could theoretically occur within natural 4H-SiC.

To summarize this section, eight of the ten 1SSF models examined were classified as stably existing defects, and six of them transformed into previously documented structures. Among the six models, D_{14}, D_{24}, D_{15}, and D_{25} adopted the configuration of 30° PDs, and D_{13} and D_{23} formed the structures of 90° PDs. Apart from the mis-stacking of atomic layers caused by 30° and 90° PDs, the 90° PDs also resulted

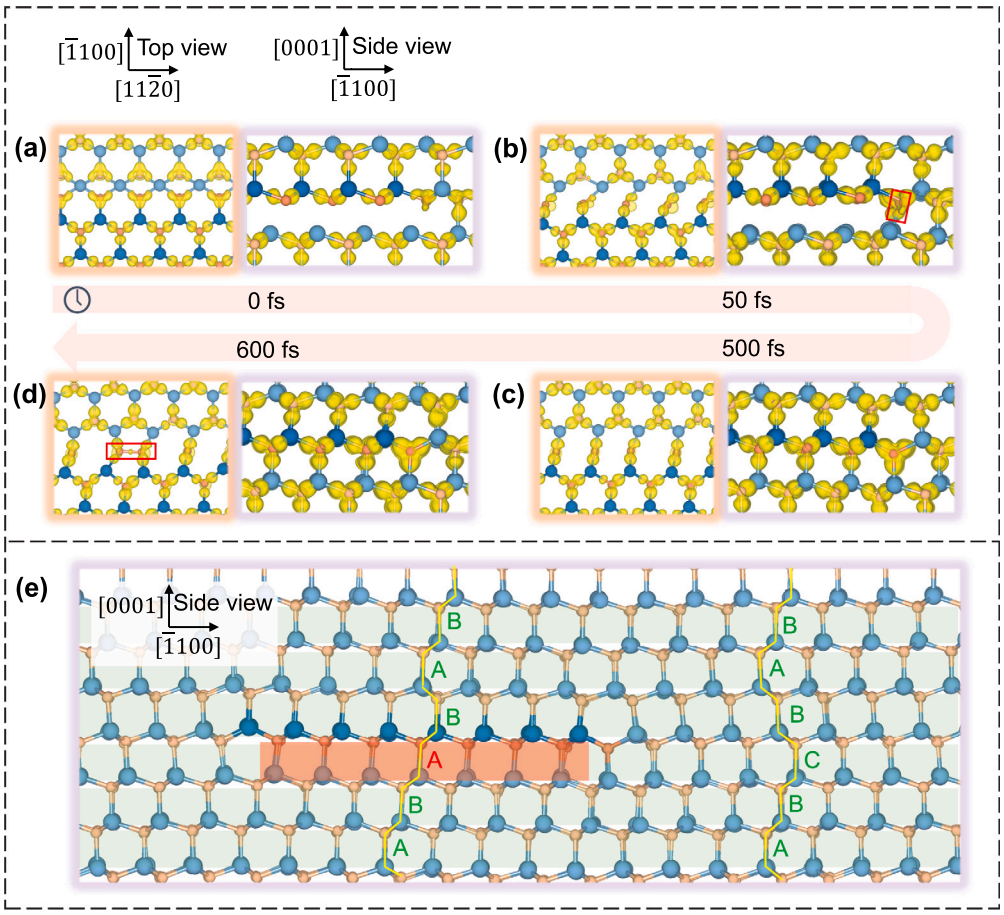

Fig. 6. The evolution of D_{14} in the 300 K simulation. The viewpoints were similar to Fig. 5. (a)–(d) The top view and side view at 0 fs, 50 fs, 500 fs, and 600 fs, respectively. The differential charge density is shown as a yellow isosurface to represent the values of 0.02 e/Å^3. (e) The stacking order of the atoms in the final structure. The red shadow indicates the mis-stacking atoms.

in distortions of atomic layers. Regarding thermal stability, the 90° PDs showed lower thermal stability as kink migration (along with the change of size of the 1SSF) was observed when temperature above 1200 K, but the 1SSFs with 30° PDs maintained their size at 2000 K. Our observations suggest that high-temperature annealing might not be sufficient to eliminate all BPDs especially for the 30° PDs, because the process of converting BPDs into threading edge dislocations requires the shrinkage of 1SSFs and the recombination of PDs [19]. Besides, two brand-new structures (D_{12} and D_{22}) were found, which were characterized by flipped Si and C atomic layers in the 1SSFs. These two new structures displayed high thermal stability and suggested to be potentially existing in natural 4H-SiC.

3.3. Specific vibration modes of 1SSFs on phonon spectra

After the thermal stability investigation, the vibration modes were further studied to explore the potential acoustic and optical properties of those 1SSFs. The representative examples of D_{12} and D_{14} were demonstrated comparing with the defect-free 4H-SiC (Fig. 9). Encouragingly, specific phonon modes were found that only appeared in the 1SSF models but not in the defect-free 4H-SiC. Both D_{12} and D_{14} had a phonon mode at the Γ point with a frequency of 3.2 THz (highlighted by the baby-blue boxes). This finding at the Γ point may be used in the Raman spectrum, because the Raman spectrum is usually used to measure the vibration modes at the Γ point [63]. In addition, there were certain vibration modes of 1SSFs obviously appeared within the forbidden band of 4H-SiC (18.3 THz to 21.5 THz, highlighted by the black boxes), which could also be used as an indicator to detect 1SSFs and BPDs of 4H-SiC. Our founding might pave the way to facilitate a new identification and spatial mapping of 1SSFs in 4H-SiC materials without any damage (the wet etching was not required for the Raman spectrum), similar to the attempt in our work [64], and the application of Raman requires experimental verification in the future.

4. Conclusion

In this work, an MLFF for the Si-C system was developed, and the MLFF outcomes were compared with simulations by other methods and experimental results. Subsequently, the MLFF was used to investigate the thermal stability of 1SSFs under different temperatures. APBs were found to be an important factor in the thermal stability of 1SSF, which was reflected by the disappearance of APB-lacking defects. The high thermal stability of 30° PDs were found, and the bidirectional transformation between SR and AR was observed in 30° PDs under high temperatures. Meanwhile, kink migrations were observed in 90° PDs under high temperatures. Besides, two brand-new 1SSF structures were found and they have high thermal stability, which were characterized by flipped atomic layers within the 1SSF and could theoretically occur within natural 4H-SiC. Last but not the least, the vibration modes of 1SSFs were investigated, and specific vibration modes of different 1SSFs were characterized, potentially facilitate non-destructive defect detection of 1SSFs. This work provides a comprehensive thermal-related evolution study of 1SSFs in 4H-SiC at the atomic level.

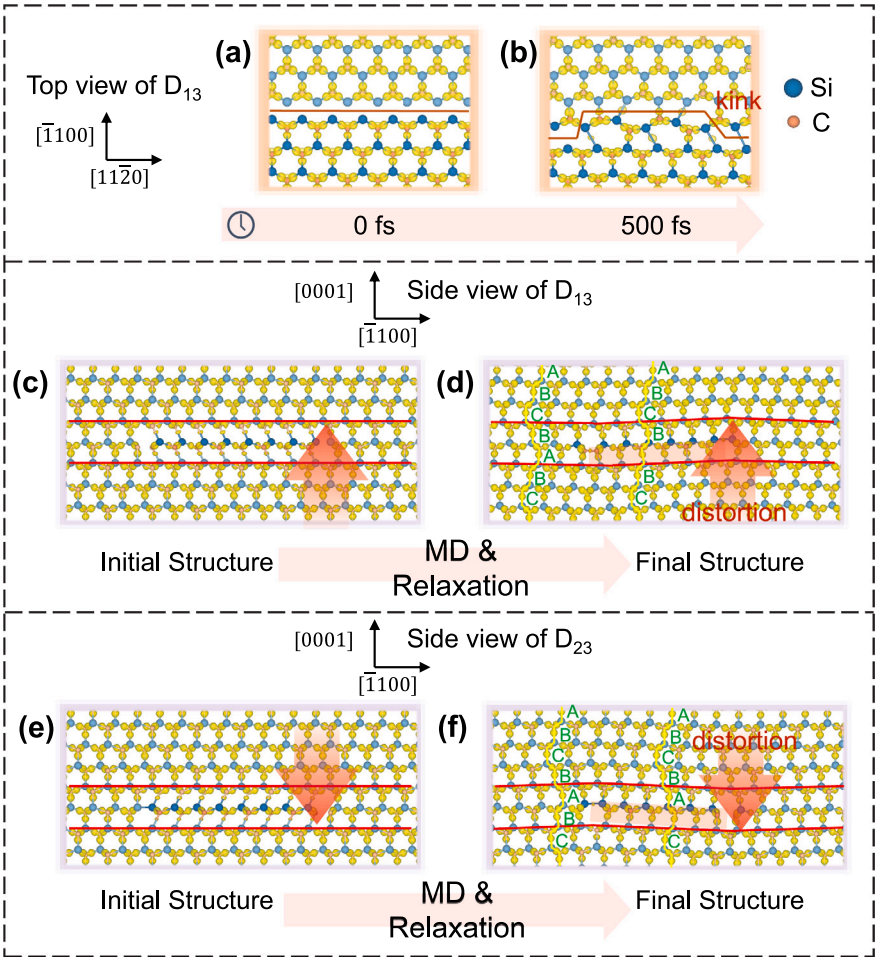

Fig. 7. The evolution of D_{13} and D_{23}. The viewpoints were similar to Fig. 5. (a)–(b) The top view of the structures in the simulation of D_{13} at 300 K. (c)–(f) The side view of the structures before and after simulation for (c)–(d) D_{13} and (e)–(f) D_{23}. The red lines indicate the Si layer adjacent to the 1SSF, and the arrows indicate the distortion of the structure. The differential charge density is shown as yellow isosurface in (a)–(f) to represent the values of 0.02 e/Å^3.

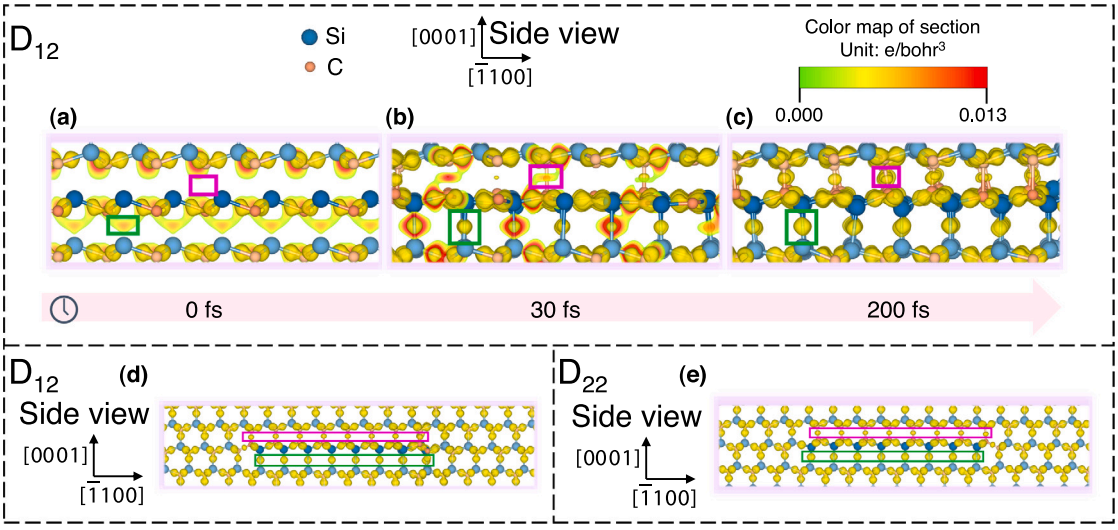

Fig. 8. (a)–(c) The side view of D_{12} in the 300 K simulation at (a) 0 fs, (b) 30 fs, and (c) 200 fs, respectively. The viewpoints were similar to Fig. 5. (d)–(e) The overview of final structures of (d) D_{12} and (e) D_{22}, respectively. The differential charge density was displayed as yellow isosurface to represent the values of 0.02 e/Å^3. In addition, two slices of different charge density distributions were placed across atomic layers to take a closer look at the charge aggregation between the layers.

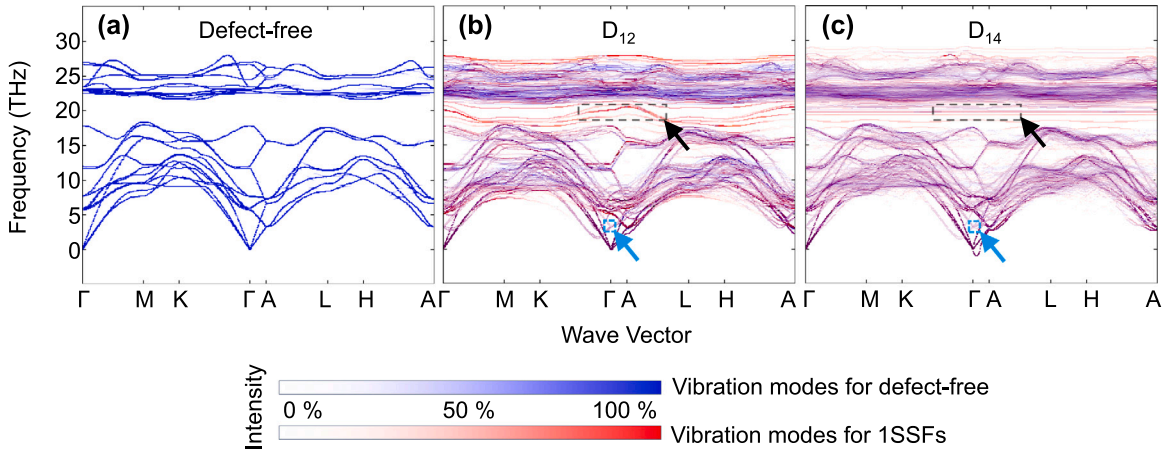

Fig. 9. Phonon spectra of (a) the defect-free model, (b) D_{12}, and (c) D_{14}. The red and blue lines correspond to the vibration modes of 1SSF and defect-free parts, respectively, and the purple lines (a combination of red and blue) represent the phonon modes shared by the two parts.

CRediT authorship contribution statement

Haonan Chen: Writing – review & editing, Writing – original draft, Visualization, Validation, Software, Methodology, Data curation, Conceptualization. **Wenyu Kang:** Writing – review & editing, Writing – original draft, Resources, Funding acquisition. **Wei Lin:** Validation, Supervision, Software, Resources, Project administration, Methodology, Investigation, Funding acquisition, Conceptualization. **Junyong Kang:** Writing – review & editing, Writing – original draft, Validation, Supervision, Software, Resources, Project administration, Methodology, Investigation, Funding acquisition, Formal analysis, Conceptualization.

Declaration of competing interest

The authors declare that they have no known competing financial interests or personal relationships that could have appeared to influence the work reported in this paper.

Data availability

Trained MLFF was available for download from Mendeley Data [65]. The program for approximately unfolding phonon spectrum was available at https://github.com/CHN-beta/ufo.

Acknowledgments

This work was supported by the National Key R&D Program of China [2021YFB3401604]; the Key Scientific and Technological Program of Xiamen [3502Z20231014 & 3502Z20231045]; and the Innovation Program for Quantum Science and Technology [2021ZD0303400]. We acknowledge the technical assistance from Leilei Xiang and Junqi Yao at Xiamen University.

Appendix A. Supplementary data

Supplementary material related to this article can be found online at https://doi.org/10.1016/j.commatsci.2024.113077.

References

[1] J.B. Casady, R.W. Johnson, Status of silicon carbide (SiC) as a wide-bandgap emiconductor for high-temperature applications: a review, Solid-State Electron. 39 (10) (1996) 1409–1422, http://dx.doi.org/10.1016/0038-1101(96)00045-7.

[2] H. Okumura, Present status and future prospect of widegap semiconductor high-power devices, Japan. J. Appl. Phys. 45 (10A) (2006) 7565–7586, http://dx.doi.org/10.1143/JJAP.45.7565.

[3] R. Cheung, Silicon carbide microelectromechanical systems for harsh environments, Imperial College Press, London, 2006, OCLC.

[4] D. Dompoint, A. Boulle, I. Galben-Sandulache, D. Chaussende, L.T.M. Hoa, T. Ouisse, D. Eyidi, J.L. Demenet, M.F. Beaufort, J. Rabier, Kinetics of the 3C-6H polytypic transition in 3C-SiC single crystals: A diffuse X-ray scattering study, J. Appl. Phys. 110 (5) (2011) 053508, http://dx.doi.org/10.1063/1.3627371.

[5] V.A. Izhevskyi, L.A. Genova, J.C. Bressiani, A.H.A. Bressiani, Review article: silicon carbide. structure, properties and processing, Cerâmica 46 (297) (2000) 4–13, http://dx.doi.org/10.1590/S0366-69132000000100002.

[6] T. Kimoto, Bulk and epitaxial growth of silicon carbide, Prog. Cryst. Growth Charact. Mater. 62 (2) (2016) 329–351, http://dx.doi.org/10.1016/j.pcrysgrow.2016.04.018.

[7] C.Y. Tang, F.H. Li, R. Wang, J. Zou, X.H. Zheng, J.W. Liang, Atomic configurations of dislocation core and twin boundaries in 3C-SiC studied by high-resolution electron microscopy, Phys. Rev. B 75 (18) (2007) 184103, http://dx.doi.org/10.1103/PhysRevB.75.184103.

[8] A.T. Blumenau, T.A.G. Eberlein, R. Jones, S. Öberg, T. Frauenheim, P.R. Briddon, The effect of charge on kink migration at 90° partial dislocations in SiC, Phys. Status Solidi 202 (5) (2005) 877–882, http://dx.doi.org/10.1002/pssa.200460504.

[9] F. Bernardini, L. Colombo, Interaction of doping impurities with the 30° partial dislocations in SiC: An *ab initio* investigation, Phys. Rev. B 72 (8) (2005) 085215, http://dx.doi.org/10.1103/PhysRevB.72.085215.

[10] D. Rodney, L. Ventelon, E. Clouet, L. Pizzagalli, F. Willaime, Ab initio modeling of dislocation core properties in metals and semiconductors, Acta Mater. 124 (2017) 633–659, http://dx.doi.org/10.1016/j.actamat.2016.09.049.

[11] A.T. Blumenau, C.J. Fall, R. Jones, M.I. Heggie, P.R. Briddon, T. Frauenheim, S. Berg, Straight and kinked 90° partial dislocations in diamond and 3C-SiC, J. Phys.: Condens. Matter 14 (48) (2002) 12741–12747, http://dx.doi.org/10.1088/0953-8984/14/48/311.

[12] A.T. Blumenau, C.J. Fall, R. Jones, S. Öberg, T. Frauenheim, P.R. Briddon, Structure and motion of basal dislocations in silicon carbide, Phys. Rev. B 68 (17) (2003) 174108, http://dx.doi.org/10.1103/PhysRevB.68.174108.

[13] P. Vashishta, R.K. Kalia, A. Nakano, J.P. Rino, Interaction potential for silicon carbide: A molecular dynamics study of elastic constants and vibrational density of states for crystalline and amorphous silicon carbide, J. Appl. Phys. 101 (10) (2007) 103515, http://dx.doi.org/10.1063/1.2724570.

[14] H. Tsuchida, I. Kamata, T. Miyazawa, M. Ito, X. Zhang, M. Nagano, Recent advances in 4H-SiC epitaxy for high-voltage power devices, Mater. Sci. Semicond. Process. 78 (2018) 2–12, http://dx.doi.org/10.1016/j.mssp.2017.11.003.

[15] S. Harada, T. Mii, H. Sakane, M. Kato, Suppression of stacking fault expansion in a 4H-SiC epitaxial layer by proton irradiation, Sci. Rep. 12 (1) (2022) 13542, http://dx.doi.org/10.1038/s41598-022-17060-y.

[16] Y. Sun, W. Kang, H. Chen, X. Chen, Y. Dong, W. Lin, J. Kang, Selection of growth monomers on the 4H-SiC (0001) atomic step surfaces: from the first-principles calculations to homo-epitaxy verification, Appl. Surf. Sci. 606 (2022) 154949, http://dx.doi.org/10.1016/j.apsusc.2022.154949.

[17] M. Bhatnagar, B. Baliga, Comparison of 6H-SiC, 3C-SiC, and Si for power devices, IEEE Trans. Electron Devices 40 (3) (1993) 645–655, http://dx.doi.org/10.1109/16.199372.

[18] T. Kimoto, Material science and device physics in SiC technology for high-voltage power devices, Japan. J. Appl. Phys. 54 (4) (2015) 040103, http://dx.doi.org/10.7567/JJAP.54.040103.

[19] J. Nishio, A. Okada, C. Ota, M. Kushibe, Triangular single shockley stacking fault analyses on 4H-SiC PiN diode with forward voltage degradation, J. Electron. Mater. 49 (9) (2020) 5232–5239, http://dx.doi.org/10.1007/s11664-020-08133-7.

[20] N.A. Mahadik, R.E. Stahlbush, J.D. Caldwell, K.D. Hobart, Ultraviolet photoluminescence imaging of stacking fault contraction in 4H-SiC epitaxial layers, Mater. Sci. Forum 717–720 (2012) 391–394, http://dx.doi.org/10.4028/www.scientific.net/MSF.717-720.391.

[21] M.H. Hong, A.V. Samant, P. Pirouz, Stacking fault energy of 6H-SiC and 4H-SiC single crystals, Phil. Mag. A 80 (4) (2000) 919–935, http://dx.doi.org/10.1080/01418610008212090.

[22] J.L. Demenet, X. Milhet, J. Rabier, TEM observations of the coexistence of perfect and dissociated dislocations in SiC under high stress, Phys. Status Solidi C: Curr. Top. Solid State Phys. 2 (6) (2005) 1987–1991, http://dx.doi.org/10.1002/pssc.200460541.

[23] A. Okada, J. Nishio, R. Iijima, C. Ota, A. Goryu, M. Miyazato, M. Ryo, T. Shinohe, M. Miyajima, T. Kato, Y. Yonezawa, H. Okumura, Dependences of contraction/expansion of stacking faults on temperature and current density in 4H-SiC p-i-n diodes, Japan. J. Appl. Phys. 57 (6) (2018) 061301, http://dx.doi.org/10.7567/JJAP.57.061301.

[24] Y. Iwahashi, M. Miyazato, M. Miyajima, Y. Yonezawa, T. Kato, H. Fujiwara, K. Hamada, A. Otsuki, H. Okumura, Extension of stacking faults in 4H-SiC pn diodes under a high current pulse stress, Mater. Sci. Forum 897 (2017) 218–221, http://dx.doi.org/10.4028/www.scientific.net/MSF.897.218.

[25] J.D. Caldwell, R.E. Stahlbush, M.G. Ancona, O.J. Glembocki, K.D. Hobart, On the driving force for recombination-induced stacking fault motion in 4H-SiC, J. Appl. Phys. 108 (4) (2010) 044503, http://dx.doi.org/10.1063/1.3467793.

[26] T. Miyanagi, H. Tsuchida, I. Kamata, T. Nakamura, K. Nakayama, R. Ishii, Y. Sugawara, Annealing effects on single shockley faults in 4H-SiC, Appl. Phys. Lett. 89 (6) (2006) 062104, http://dx.doi.org/10.1063/1.2234740.

[27] A. Iijima, I. Kamata, H. Tsuchida, J. Suda, T. Kimoto, Correlation between shapes of shockley stacking faults and structures of basal plane dislocations in 4H-SiC epilayers, Phil. Mag. 97 (30) (2017) 2736–2752, http://dx.doi.org/10.1080/14786435.2017.1350788.

[28] J.D. Caldwell, R.E. Stahlbush, E.A. Imhoff, K.D. Hobart, M.J. Tadjer, Q. Zhang, A. Agarwal, Recombination-induced stacking fault degradation of 4H-SiC merged-PiN-Schottky diodes, J. Appl. Phys. 106 (4) (2009) 044504, http://dx.doi.org/10.1063/1.3194323.

[29] G. Savini, M.I. Heggie, S. Öberg, Core structures and kink migrations of partial dislocations in 4H-SiC, Faraday Discuss. 134 (2007) 353–367, http://dx.doi.org/10.1039/B603920K.

[30] K.X. Liu, R.E. Stahlbush, S.I. Maximenko, J.D. Caldwell, Differences in emission spectra of Si- and C-core partial dislocations, Appl. Phys. Lett. 90 (15) (2007) 153503, http://dx.doi.org/10.1063/1.2721139.

[31] T. Hahn, Printed symbols for crystallographic items, in: H. Fuess, T. Hahn, H. Wondratschek, U. Müller, U. Shmueli, E. Prince, A. Authier, V. Kopský, D.B. Litvin, M.G. Rossmann, E. Arnold, S. Hall, B. McMahon, T. Hahn (Eds.), International Tables for Crystallography, A, first ed., International Union of Crystallography, Chester, England, 2006, pp. 2–3, http://dx.doi.org/10.1107/97809553602060000500.

[32] R.C. Powell, Symmetry, group theory, and the physical properties of crystals, in: Lecture Notes in Physics, vol. 824, Springer New York, New York, 2010.

[33] K. Momma, F. Izumi, *VESTA 3* for three-dimensional visualization of crystal, volumetric and morphology data, J. Appl. Crystallogr. 44 (6) (2011) 1272–1276, http://dx.doi.org/10.1107/S0021889811038970.

[34] G. Kresse, J. Furthmüller, Efficiency of ab-initio total energy calculations for metals and semiconductors using a plane-wave basis set, Comput. Mater. Sci. 6 (1) (1996) 15–50, http://dx.doi.org/10.1016/0927-0256(96)00008-0.

[35] C.M. Bishop, Pattern recognition and machine learning, in: Information science and statistics, Springer, New York, 2006.

[36] R. Jinnouchi, F. Karsai, G. Kresse, On-the-fly machine learning force field generation: Application to melting points, Phys. Rev. B 100 (1) (2019) 014105, http://dx.doi.org/10.1103/PhysRevB.100.014105.

[37] R. Jinnouchi, F. Karsai, C. Verdi, R. Asahi, G. Kresse, Descriptors representing two- and three-body atomic distributions and their effects on the accuracy of machine-learned inter-atomic potentials, J. Chem. Phys. 152 (23) (2020) 234102, http://dx.doi.org/10.1063/5.0009491.

[38] Machine learning force field: Theory - Vaspwiki.

[39] M.W. Mahoney, P. Drineas, CUR matrix decompositions for improved data analysis, Proc. Natl. Acad. Sci. 106 (3) (2009) 697–702, http://dx.doi.org/10.1073/pnas.0803205106.

[40] R. Jinnouchi, J. Lahnsteiner, F. Karsai, G. Kresse, M. Bokdam, Phase transitions of hybrid perovskites simulated by machine-learning force fields trained on the fly with Bayesian inference, Phys. Rev. Lett. 122 (22) (2019) 225701, http://dx.doi.org/10.1103/PhysRevLett.122.225701.

[41] M. Parrinello, A. Rahman, Polymorphic transitions in single crystals: a new molecular dynamics method, J. Appl. Phys. 52 (12) (1981) 7182–7190, http://dx.doi.org/10.1063/1.328693.

[42] M.P. Allen, D.J. Tildesley, Computer simulation of liquids, second ed., Oxford University Press, Oxford, United Kingdom, 2017.

[43] M. Ernzerhof, G.E. Scuseria, Assessment of the Perdew-Burke-Ernzerhof exchange-correlation functional, J. Chem. Phys. 110 (11) (1999) 5029–5036, http://dx.doi.org/10.1063/1.478401.

[44] G. Kresse, D. Joubert, From ultrasoft pseudopotentials to the projector augmented-wave method, Phys. Rev. B 59 (3) (1999) 1758–1775, http://dx.doi.org/10.1103/PhysRevB.59.1758.

[45] A.P. Thompson, H.M. Aktulga, R. Berger, D.S. Bolintineanu, W.M. Brown, P.S. Crozier, P.J. in 't Veld, A. Kohlmeyer, S.G. Moore, T.D. Nguyen, R. Shan, M.J. Stevens, J. Tranchida, C. Trott, S.J. Plimpton, LAMMPS - a flexible simulation tool for particle-based materials modeling at the atomic, meso, and continuum scales, Comput. Phys. Comm. 271 (2022) 108171, http://dx.doi.org/10.1016/j.cpc.2021.108171.

[46] J. Tersoff, Modeling solid-state chemistry: Interatomic potentials for multicomponent systems, Phys. Rev. B 39 (8) (1989) 5566–5568, http://dx.doi.org/10.1103/PhysRevB.39.5566.

[47] J. Tersoff, Carbon defects and defect reactions in silicon, Phys. Rev. Lett. 64 (15) (1990) 1757–1760, http://dx.doi.org/10.1103/PhysRevLett.64.1757.

[48] J. Tersoff, Chemical order in amorphous silicon carbide, Phys. Rev. B 49 (23) (1994) 16349–16352, http://dx.doi.org/10.1103/PhysRevB.49.16349.

[49] P. Erhart, K. Albe, Analytical potential for atomistic simulations of silicon, carbon, and silicon carbide, Phys. Rev. B 71 (3) (2005) 035211, http://dx.doi.org/10.1103/PhysRevB.71.035211.

[50] F. Gao, W.J. Weber, Empirical potential approach for defect properties in 3C-SiC, Nucl. Instrum. Methods Phys. Res. B 191 (1–4) (2002) 504–508, http://dx.doi.org/10.1016/S0168-583X(02)00600-6.

[51] J.F. Ziegler, J.P. Biersack, The Stopping and Range of Ions in Matter, Springer US, Boston, MA, 1985,

[52] M.I. Baskes, Modified embedded-atom potentials for cubic materials and impurities, Phys. Rev. B 46 (5) (1992) 2727–2742, http://dx.doi.org/10.1103/PhysRevB.46.2727.

[53] H. Huang, N.M. Ghoniem, J.K. Wong, M. Baskes, Molecular dynamics determination of defect energetics in beta -SiC using three representative empirical potentials, Modelling Simul. Mater. Sci. Eng. 3 (5) (1995) 615–627, http://dx.doi.org/10.1088/0965-0393/3/5/003.

[54] K.-H. Kang, T. Eun, M.-C. Jun, B.-J. Lee, Governing factors for the formation of 4H or 6H-SiC polytype during SiC crystal growth: An atomistic computational approach, J. Cryst. Growth 389 (2014) 120–133, http://dx.doi.org/10.1016/j.jcrysgro.2013.12.007.

[55] G. Lucas, M. Bertolus, L. Pizzagalli, An environment-dependent interatomic potential for silicon carbide: calculation of bulk properties, high-pressure phases, point and extended defects, and amorphous structures, J. Phys.: Condens. Matter 22 (3) (2010) 035802, http://dx.doi.org/10.1088/0953-8984/22/3/035802.

[56] Y. Le Page, P. Saxe, Symmetry-general least-squares extraction of elastic data for strained materials from *ab initio* calculations of stress, Phys. Rev. B 65 (10) (2002) 104104, http://dx.doi.org/10.1103/PhysRevB.65.104104.

[57] X. Wu, D. Vanderbilt, D.R. Hamann, Systematic treatment of displacements, strains, and electric fields in density-functional perturbation theory, Phys. Rev. B 72 (3) (2005) 035105, http://dx.doi.org/10.1103/PhysRevB.72.035105.

[58] K. Kamitani, M. Grimsditch, J.C. Nipko, C.-K. Loong, M. Okada, I. Kimura, The elastic constants of silicon carbide: A brillouin-scattering study of 4H and 6H SiC single crystals, J. Appl. Phys. 82 (6) (1997) 3152–3154, http://dx.doi.org/10.1063/1.366100.

[59] A. Togo, I. Tanaka, First principles phonon calculations in materials science, Scr. Mater. 108 (2015) 1–5, http://dx.doi.org/10.1016/j.scriptamat.2015.07.021.

[60] A. Togo, First-principles phonon calculations with phonopy and phono3py, J. Phys. Soc. Japan 92 (1) (2023) 012001, http://dx.doi.org/10.7566/JPSJ.92.012001.

[61] J.F. Nye, Physical properties of crystals: their representation by tensors and matrices, first ed., Oxford University Press, New York, 1984.

[62] F. Zheng, P. Zhang, Phonon dispersion unfolding in the presence of heavy breaking of spatial translational symmetry, Comput. Mater. Sci. 125 (2016) 218–223, http://dx.doi.org/10.1016/j.commatsci.2016.08.036.

[63] Z.C. Feng, D. Zhao, L. Wan, W. Lu, J. Yiin, B. Klein, I.T. Ferguson, Angle-dependent Raman scattering studies on anisotropic properties of crystalline hexagonal 4H-SiC, Materials 15 (24) (2022) 8751, http://dx.doi.org/10.3390/ma15248751.

[64] X. Ye, A. Zhang, J. Huang, W. Kang, W. Jiang, X. Li, J. Yin, J. Kang, Non-destructive and deep learning-enhanced characterization of 4H-SiC material, Aggregate (2024) e524, http://dx.doi.org/10.1002/agt2.524.

[65] H. Chen, SiC-1SSF-MLFF, 2024, http://dx.doi.org/10.17632/H8JSF45SKC.1.